Improved measurements of the β-decay response of liquid xenon with the LUX detector

D. S. Akerib,[1,2,3] S. Alsum,[4] H. M. Araújo,[5] X. Bai,[6] J. Balajthy,[7,8] A. Baxter,[9] P. Beltrame,[10] E. P. Bernard,[11] A. Bernstein,[12] T. P. Biesiadzinski,[1,2,3] E. M. Boulton,[11,13,14] B. Boxer,[9] P. Brás,[15] S. Burdin,[9] D. Byram,[16,17] M. C. Carmona-Benitez,[18] C. Chan,[19] J. E. Cutter,[8] L. de Viveiros,[18] E. Druszkiewicz,[20] S. R. Fallon,[21] A. Fan,[2,3] S. Fiorucci,[13,19] R. J. Gaitskell,[19] J. Genovesi,[21] C. Ghag,[22] M. G. D. Gilchriese,[13] C. Gwilliam,[9] C. R. Hall,[7] S. J. Haselschwardt,[23] S. A. Hertel,[24,13] D. P. Hogan,[11] M. Horn,[17,11] D. Q. Huang,[19] C. M. Ignarra,[2,3] R. G. Jacobsen,[11] O. Jahangir,[22] W. Ji,[1,2,3] K. Kamdin,[11,13] K. Kazkaz,[12] D. Khaitan,[20] E. V. Korolkova,[25] S. Kravitz,[13] V. A. Kudryavtsev,[25] E. Leason,[10] B. G. Lenardo,[8,12] K. T. Lesko,[13] J. Liao,[19] J. Lin,[11] A. Lindote,[15] M. I. Lopes,[15] A. Manalaysay,[8] R. L. Mannino,[26,4] N. Marangou,[5] M. F. Marzioni,[10] D. N. McKinsey,[11,13] D.-M. Mei,[16] M. Moongweluwan,[20] J. A. Morad,[8] A. St. J. Murphy,[10] A. Naylor,[25] C. Nehrkorn,[23] H. N. Nelson,[23] F. Neves,[15] A. Nilima,[10] K. C. Oliver-Mallory,[11,13] K. J. Palladino,[4] E. K. Pease,[11,13] Q. Riffard,[11,13] G. R. C. Rischbieter,[21] C. Rhyne,[19] P. Rossiter,[25] S. Shaw,[23,22] T. A. Shutt,[1,2,3] C. Silva,[15] M. Solmaz,[23] V. N. Solovov,[15] P. Sorensen,[13] T. J. Sumner,[5] M. Szydagis,[21] D. J. Taylor,[17] R. Taylor,[5] W. C. Taylor,[19] B. P. Tennyson,[14] P. A. Terman,[26] D. R. Tiedt,[6] W. H. To,[27] M. Tripathi,[8] L. Tvrznikova,[11,13,14] U. Utku,[22] S. Uvarov,[8] A. Vacheret,[5] V. Velan,[11] R. C. Webb,[26] J. T. White,[26] T. J. Whitis,[1,2,3] M. S. Witherell,[13] F. L. H. Wolfs,[20] D. Woodward,[18] J. Xu,[12] and C. Zhang[16]

(LUX Collaboration)

[1]*Case Western Reserve University, Department of Physics, 10900 Euclid Avenue, Cleveland, Ohio 44106, USA*
[2]*SLAC National Accelerator Laboratory, 2575 Sand Hill Road, Menlo Park, California 94205, USA*
[3]*Kavli Institute for Particle Astrophysics and Cosmology, Stanford University, 452 Lomita Mall, Stanford, California 94309, USA*
[4]*University of Wisconsin-Madison, Department of Physics, 1150 University Avenue, Madison, Wisconsin 53706, USA*
[5]*Imperial College London, High Energy Physics, Blackett Laboratory, London SW7 2BZ, United Kingdom*
[6]*South Dakota School of Mines and Technology, 501 East St Joseph Street, Rapid City, South Dakota 57701, USA*
[7]*University of Maryland, Department of Physics, College Park, Maryland 20742, USA*
[8]*University of California Davis, Department of Physics, One Shields Avenue, Davis, California 95616, USA*
[9]*University of Liverpool, Department of Physics, Liverpool L69 7ZE, United Kingdom*
[10]*SUPA, School of Physics and Astronomy, University of Edinburgh, Edinburgh EH9 3FD, United Kingdom*
[11]*University of California Berkeley, Department of Physics, Berkeley, California 94720, USA*
[12]*Lawrence Livermore National Laboratory, 7000 East Avenue, Livermore, California 94551, USA*
[13]*Lawrence Berkeley National Laboratory, 1 Cyclotron Road, Berkeley, California 94720, USA*
[14]*Yale University, Department of Physics, 217 Prospect Street, New Haven, Connecticut 06511, USA*
[15]*LIP-Coimbra, Department of Physics, University of Coimbra, Rua Larga, 3004-516 Coimbra, Portugal*
[16]*University of South Dakota, Department of Physics, 414E Clark Street, Vermillion, South Dakota 57069, USA*
[17]*South Dakota Science and Technology Authority, Sanford Underground Research Facility, Lead, South Dakota 57754, USA*
[18]*Pennsylvania State University, Department of Physics, 104 Davey Lab, University Park, Pennsylvania 16802-6300, USA*
[19]*Brown University, Department of Physics, 182 Hope Street, Providence, Rhode Island 02912, USA*
[20]*University of Rochester, Department of Physics and Astronomy, Rochester, New York 14627, USA*
[21]*University at Albany, State University of New York, Department of Physics, 1400 Washington Avenue, Albany, New York 12222, USA*
[22]*Department of Physics and Astronomy, University College London, Gower Street, London WC1E 6BT, United Kingdom*
[23]*University of California Santa Barbara, Department of Physics, Santa Barbara, California 93106, USA*
[24]*University of Massachusetts, Amherst Center for Fundamental Interactions and Department of Physics, Amherst, Massachusetts 01003-9337 USA*

[25]*University of Sheffield, Department of Physics and Astronomy, Sheffield, S3 7RH, United Kingdom*
[26]*Texas A & M University, Department of Physics, College Station, Texas 77843, USA*
[27]*California State University Stanislaus, Department of Physics, 1 University Circle, Turlock, California 95382, USA*

(Received 2 April 2019; published 10 July 2019)

We report results from an extensive set of measurements of the β-decay response in liquid xenon. These measurements are derived from high-statistics calibration data from injected sources of both ^{3}H and ^{14}C in the LUX detector. The mean light-to-charge ratio is reported for 13 electric field values ranging from 43 to 491 V/cm, and for energies ranging from 1.5 to 145 keV.

DOI: 10.1103/PhysRevD.100.022002

I. INTRODUCTION

The Large Underground Xenon experiment (LUX) was a liquid-xenon (LXe) time-projection chamber (TPC). Before it was decommissioned in 2016, LUX was located in the Davis cavern of the Sanford Underground Research Facility (SURF) in Lead, South Dakota, on the 4,850' level [1]. In total, it contained about 370 kg of xenon, 250 kg of which was active. Energy deposits in the sensitive volume were detected using two arrays of 61 photomultiplier tubes (PMTs) at the top and bottom of the detector.

LUX was initially designed as a weakly interacting massive particle (WIMP) dark-matter detector. The LUX full exposure of 3.35×10^4 kg days combines the first data-taking run (WS2013), which took place from April to August 2013 [2,3], with the second data-taking run (WS2014-2016), which ran from September 2014 until May 2016 [4]. A 50 GeV/c^2 WIMP with a cross section greater than 1.1×10^{-46} cm^2 is excluded with 90% confidence. Recently, stronger limits have been placed by the XENON-1T and PandaX experiments [5,6].

As a two-phase TPC, LUX was sensitive to light and charge signals via primary ($S1$) and secondary ($S2$) scintillation, respectively. The light and charge yields (Ly and Qy) are defined as the average number of quanta (photons and electrons) per keV of energy deposited in the LXe. These depend upon the energy of the event, the magnitude of the electric field applied at the event's location, and whether the interaction leads to a nuclear recoil (NR) or an electron recoil (ER). The yields of an electron recoil may also depend upon further specifics of the interaction. For instance, interactions of β particles in LXe may produce different yields from those of gammas, because the latter has some energy-dependent probability of photoabsorption, while the former does not [7]. Such variations will be seen in Sec. V B when comparing values of Qy from β interactions with those from ^{83m}Kr and ^{131m}Xe decays.

The most prevalent and problematic backgrounds in current and future LXe dark-matter experiments are β decays of Rn daughters [5,6,8,9]. It is therefore important to understand the β-decay-induced light and charge yields in LXe as a function of electric field and energy. Previous measurements of these yields using LUX WS2013 data, including a set of measurements using a ^{3}H injection source at both 105 and 180 V/cm were reported in Refs. [10–12]. In this article we use the data from a novel ^{14}C injection and a high-statistics ^{3}H calibration, which were conducted after WS2014-2016, to extend the previous results over a much wider range of energies and electric fields.

The electric field in the WS2014-2016 LUX detector was highly nonuniform, ranging from less than 50 to over 500 V/cm. In this article we divide the detector into thirteen electric field bins, with central values spanning from 43 to 491 V/cm, and obtain measurements of the light and charge yields for each associated field value [13]. The use of a ^{14}C injection source in addition to ^{3}H increases the energy range of our measurements by nearly an order of magnitude. The radioactive isotope ^{14}C β decays to the ground state of ^{14}N with a Q-value of 156 keV, which is 8.6 times greater than the ^{3}H Q-value of 18.1 keV [10,14,15].

The ^{14}C calibration was performed at the end of the LUX operational lifetime and just before decommissioning in September 2016. We refer to this period as "post-WS." The activities used in post-WS calibrations were allowed to be significantly greater than previous calibrations because maintaining low detector backgrounds was no longer a requirement. This resulted in a data set of roughly 2 million ^{14}C events. After fiducial cuts, each of the thirteen electric field bins has between 60,000 and 120,000 events. A separate post-WS ^{3}H data set is also analyzed, which has about one third of the number of events as the ^{14}C set.

II. DATA SELECTION

An interaction in the sensitive LXe produces primary scintillation photons and ionization electrons. The primary scintillation is collected by the PMTs and constitutes the $S1$ signal. The electrons are transported through an electric drift field to the top of the detector, where the electrons are extracted from the liquid surface into a region of gaseous xenon and produce the $S2$ signal through

electroluminescence. The $S2$ signal is proportional to the number of electrons extracted.

The low-energy electronic depositions studied in this work have very short track lengths (~0.3 mm) [16], and are treated as occurring at points in space. The signals caused by these depositions therefore have a single $S1$ followed by a single $S2$. The $S2$ light generated by an extracted electron is highly localized in the x-y plane at the top of the detector, so the x-y position of an event can be reconstructed by analyzing the relative size of the pulses in the top PMT array. The drifting electrons take many microseconds longer to reach the liquid surface than the $S1$ photons take to be detected. The resulting difference in time between the $S1$ and $S2$ is referred to as the "drift time." In a detector with a uniform electric drift field, the electrons drift vertically at a constant velocity, so drift time gives a direct measurement of the z-position of an event [17].

The charge and light collection efficiencies have some dependence upon position due to the attachment of drifting electrons to impurities and detector geometry. These effects are measured using the response to ^{83m}Kr and ^{3}H [4]. A new set of efficiency-corrected data has been produced in which these effects are corrected for. In this article, $S1$ and $S2$ refer to these corrected values unless otherwise specified.

To avoid edge effects in our analysis, we reject events near the boundaries of the sensitive volume. Events within about 3 cm from the walls of the detector were rejected using a radial cut, which is described in Sec. 4.2.2 of Ref. [13]. For the same reason, events with drift times greater than 330 μs or less than 10 μs were also rejected.

The simplest selection cut used to isolate single site events is to reject any event that does not contain exactly one $S1$ and one $S2$, with the $S1$ occurring before the $S2$. The efficiency of this cut is found to decrease at higher energies due to correlated pileup in both $S1$ and $S2$. In this work we use a modified version of this cut, which is described in detail in Sec. 4.2.1 of Ref. [13]. We require a selected event have at least one $S2$, and at least one $S1$ before the first $S2$. The first $S1$ and $S2$ pulses are required to contain at least 93% of the total $S1$ and $S2$ area, respectively. This modified selection cut increases the acceptance of ^{131m}Xe events from 61% to 92%, and improves the acceptance of ^{14}C events to more than 90% across the entire energy spectrum [13]. We use ^{131m}Xe as a test of our selection cut because it is a monoenergetic peak at 163.9 keV, just above the ^{14}C Q-value. The background rate remains very small in comparison to the injected sources, so the additional leakage of noise events due to the relaxed cut is negligible.

During and after WS2014-2016, the electric fields in LUX were highly nonuniform. A comprehensive study of the drift field was performed and is detailed in Ref. [18]. This study produced high-resolution maps of the electric field. Using a three-dimensional linear interpolation of these maps, we assign a specific field value to every event in our data sets. This enables us to define 13 bins in the electric field whose centers range from 43 to 491 V/cm, and where each bin extends 10% above and below its central value. We also limit the range of drift times that are drawn from so that a bin does not extend past the central drift-time values of its adjacent bins. These bins are described in greater detail in Sec. 4.2.3 of Ref. [13].

III. CALIBRATION SOURCE INJECTIONS

After WS2014-2016 was completed in June of 2016, the detector was exercised with a variety of ER and NR calibration sources. The usual ER calibrations of ^{83m}Kr [19–21] and tritiated methane (CH_3 T) [10] were performed, along with NR calibrations using the deuterium-deuterium (DD) neutron generator [22,23]. In addition to these standard calibrations, novel techniques and sources were implemented. The timeline and activities of these injections can be seen in Fig. 1.

A. ^{131m}Xe and ^{37}Ar

The isotope ^{131m}Xe deexcites through a gamma transition to its ground state with an energy of 163.93 keV and a half life of 11.84 days. It is generated using a commercially available ^{131}I pill and is introduced into the primary xenon circulation path using the ^{3}H injection system described in Ref. [10].

An injection of ^{37}Ar was also deployed. This isotope decays via electron capture to ^{37}Cl with a half-life of 35 days. In 90% of these decays, a K-shell electron is captured, followed by the emission of x rays and Auger electrons which total to 2.82 keV. There are also nonzero branching ratios for the capture of L- and M-shell electrons.

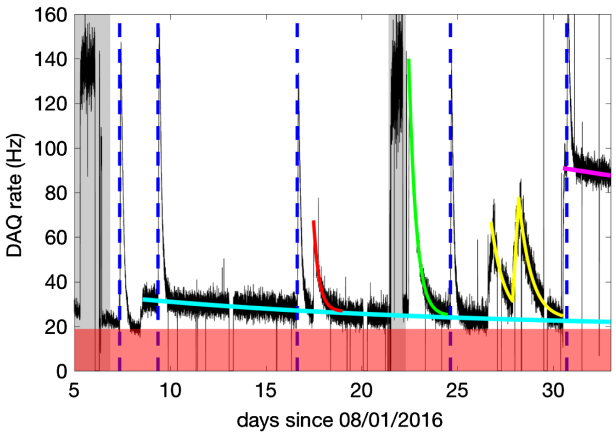

FIG. 1. The black line shows the data acquisition rate for the post-WS injection campaign. The red shaded region shows the constant baseline, while the grey shaded regions show the DD NR-calibration campaign. The vertical dashed blue lines show the times of standard ^{83m}Kr injections. The cyan, red, green, and magenta lines trace the activities following the ^{131m}Xe, ^{3}H, ^{14}C, and ^{37}Ar, respectively. Additionally, the yellow lines indicate injections of ^{220}Rn, which are not detailed in the text.

^{37}Ar can be produced through stimulated α emission of a ^{40}Ca target using a neutron beam. The ^{37}Ar sample used in LUX was produced by irradiating an aqueous solution of $CaCl_2$ with neutrons from an AmBe source. The gas above this solution was then collected and purified to obtain the gaseous sample of ^{37}Ar [24]. This sample was injected into the LUX xenon circulation using the same system as the ^{83m}Kr calibrations [20].

B. ^{14}C and ^{3}H

The ^{3}H injection system and procedure was described in detail in Ref. [10]. In the post-WS injection campaign, it was used to deploy a high-statistics ^{3}H injection, as well as a novel ^{14}C injection into the LUX detector. The ^{14}C was in the form of radiolabeled methane which is chemically identical to the tritiated methane used in Ref. [10] and was also synthesized by Moravek Biochemical [25]. The methane, and therefore the ^{14}C activity, is removed from the LUX xenon in the same manner as ^{3}H via circulation through a heated zirconium getter.

IV. MODEL OF THE LUX POST-WS β-DECAY DATA

A. Smearing of continuous β spectra

Measurements of energy-dependent parameters from continuous β spectra are affected in nontrivial ways by finite detector resolution. We obtain measurements of yields and recombination by dividing the ^{14}C and ^{3}H into reconstructed energy bins. Finite detector resolution impacts our measurements by smearing some events into a reconstructed energy bin, whose true energies lie outside of the bin. If we know both the spectral shape and the energy-dependent detector resolution, this effect can be accounted for by integrating the contribution to the ith bin from each point in the spectrum. This type of analysis was done analytically in the previous ^{3}H results [10,26]. However, the $S2$ tails described in Sec. IV D make the analytic calculations unwieldy, so in this article we perform the integration numerically using Monte Carlo (MC) data.

In order to estimate these smearing corrections, the charge and light yield is initially taken from the NEST model [7,27,28], and an initial set of MC $S1$ and $S2$ data is generated. This data set is used to make preliminary measurements of L_y and Q_y, after which the MC data are regenerated using these newly measured yields. This new set of MC data is used to remeasure the smearing corrections, giving us the final measurements of L_y and Q_y.

B. Combined energy model

We adapt the combined energy model for ER events [27,29], which relies on a simplified Platzman equation [30],

$$E_{\mathrm{ER}} = W(n_* + n_i), \tag{1}$$

where n_* is the initial number of excitons generated by an event, and n_i is the initial number of ions prior to recombination. For ER events, the work function, W, has been measured to be 13.7 ± 0.2 eV/quantum [31]. Recombination converts some ions into excitons so that the observable number of photons (n_γ) and electrons (n_e) is given by

$$\begin{aligned} n_\gamma &= n_* + r n_i \\ &= (\alpha + r) n_i \\ n_e &= (1 - r) n_i, \end{aligned} \tag{2}$$

where the exciton-ion ratio $\alpha \equiv n_*/n_i$ has been measured to be about 0.06–0.20 [26,32] for ER events and is typically assumed to be constant with energy. For ER events, we assume a constant value of $\alpha = 0.18$, which is taken from Ref. [26]. For each event, the number of ions that recombine, R, is randomly distributed about an expected value that is equal to the mean recombination probability, r, times the number of ions,

$$\langle R \rangle = r N_i. \tag{3}$$

The mean recombination probability depends on both the energy deposited and the applied electric field.

We model this process using a modified version of the NEST simulation software [7,27,28]. The total number of quanta in a simulated event (N_q) is equal to the event energy, divided by the work function. The apportionment of these quanta into exitons and ions (N_* and N_i) is treated as a binomial process, where the probability that a quantum is an ion is equal to $\frac{1}{1+\alpha}$. Recombination is modeled by drawing the number of electrons from a normal distribution with mean equal to $(1 - r) \cdot N_i$ and standard deviation equal to σ_R, where r and σ_R depend on the energy and field of the simulated event. The number of photons (N_γ) is then taken to be the number of quanta, minus the number of electrons.

C. Measuring average charge and light collection efficiencies

Reconstructed energy is an observable quantity that fluctuates around the true energy deposited in the LXe during an event. In terms of the observable $S1$ and $S2$ signals, the reconstructed energy of an event is given by

$$E_{\mathrm{rec}} = W\left(\frac{S1}{g_1} + \frac{S2}{g_2}\right), \tag{4}$$

where g_1 and g_2 are average gain factors. These values are used to convert from $S1$ to n_γ and $S2$ to n_e, accounting for the total efficiency of the detector. Equation (4) also provides a useful tool in measuring the efficiency factors, g_1 and g_2, through a method introduced by Doke *et al.* in Ref. [32].

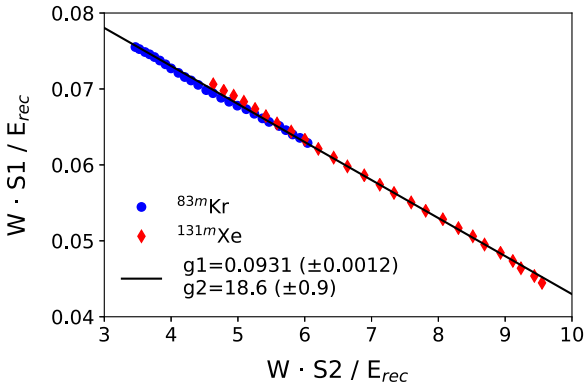

FIG. 2. Doke-style plot of post-WS ^{83m}Kr and ^{131m}Xe data. The uncertainties on the g_1 and g_2 values include systematic variation in drift time, and were calculated as described in the text. The g_1 and g_2 values are highly correlated, with a Pearson correlation coefficient of −0.90.

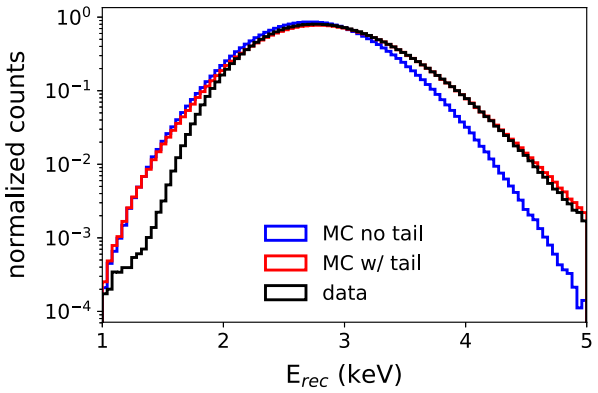

FIG. 3. Comparison of measured ^{37}Ar energy spectrum (black) versus two simulated spectra, one with the $S2$ tails modeled (red) and one without (blue). The data shown are taken from the full WIMP-search fiducial volume corresponding to electron drift times of 40 to 300 microseconds.

For a set of ER events with a constant energy E, Eq. (4) can be used to write

$$\left(\frac{W\overline{S1}}{E}\right) = -\frac{g_1}{g_2}\left(\frac{W\overline{S2}}{E}\right) + g_1, \tag{5}$$

where $\overline{S1}$ and $\overline{S2}$ are the average $S1$ and $S2$ signal observed. This linear expression may then be plotted in the usual way such that $y = (\frac{W\overline{S1}}{E})$ and $x = (\frac{W\overline{S2}}{E})$ are both in terms of either measurable quantities or known constants. The efficiency factors, g_1 and g_2, can then be obtained by fitting a line through a set of (x,y) values measured at different energies and fields.

For this analysis, the LUX post-WS values of g_1 and g_2 are measured by dividing the ^{83m}Kr and ^{131m}Xe data into separate drift-time regions and plotting the average $S1$ and $S2$ values in each region. The results of this analysis are shown in Fig. 2. To test for remaining position dependence in g_1 and g_2, we also calculate a two-point Doke plot using the ^{83m}Kr and ^{131m}Xe values from each drift-time region. The systematic uncertainty is taken to be the standard deviation of these two-point values.

The values of g_1 and g_2 we measure are $0.0931(\pm 0.0012)$, and $18.6(\pm 0.9)$, respectively. The uncertainties of these values are dominated by the systematic deviation described above. These are broadly consistent with the values found in Ref. [4], although our measured g_1 is about 3-σ below the lowest value found there. This discrepancy is likely due to a continued decrease in light collection efficiency over the three months between the end of WS2014-2016 and the beginning of the injection campaign.

D. Empirical model of $S2$ tail pathology

Figures 3 and 4 show the spectra of the ^{37}Ar and ^{131m}Xe decays measured during the post-WS calibration campaign. These combined energy spectra have clear non-Gaussian tails toward high energy. The tails in the energy spectra stem from underlying tails in the individual $S2$ spectra, which result from a pathological effect in the $S2$ signals. These $S2$ tails are much more pronounced in the WS2014-2016 and the post-WS data than in WS2013 data. The exact pathology is unknown, but there is some evidence that the tails are caused by either photoionization of impurities or "electron trains." An electron train occurs when electrons from a previous large event fail to be immediately extracted from the liquid surface and instead are emitted into the gas over a millisecond time scale.

To correctly account for smearing effects on the ^{14}C and ^{3}H spectra, we use an empirical model of the $S2$ tails. We begin with simulated $S1$ and $S2$ areas from MC events generated without tails, assuming Gaussian detector resolution. The effect of the $S2$ tails is modeled by assigning additional $S2$ area to a fraction of the simulated events.

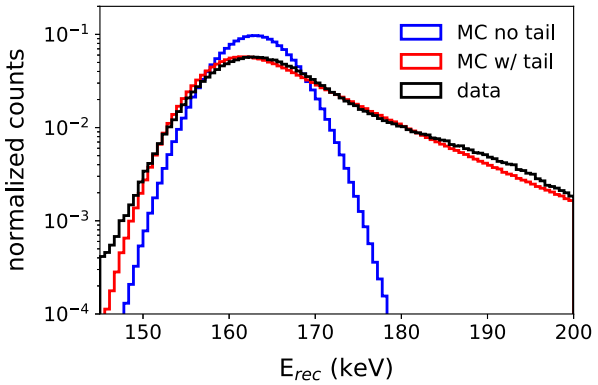

FIG. 4. Comparison of measured ^{131m}Xe energy spectrum (black) versus two simulated spectra, one with the $S2$ tails modeled (red) and one without (blue). The data shown are taken from the full WIMP-search fiducial volume corresponding to electron drift times of 40 to 300 microseconds.

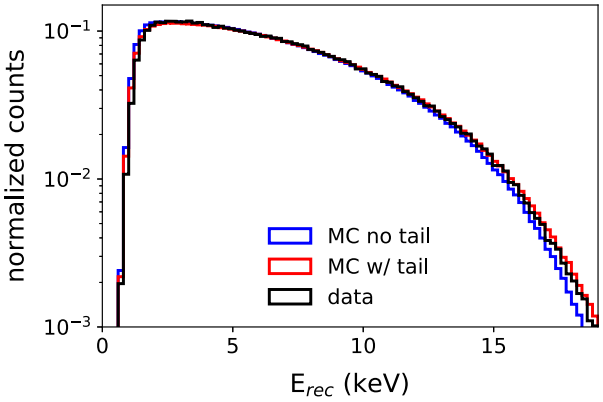

FIG. 5. Comparison of measured ^{3}H energy spectrum (black) versus two simulated spectra, one with the $S2$ tails modeled (red) and one without (blue). The data shown are taken from the full WIMP-search fiducial volume corresponding to electron drift times of 40 to 300 microseconds.

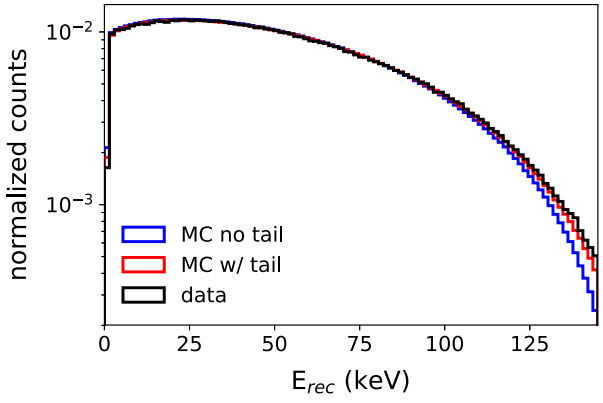

FIG. 6. Comparison of measured ^{14}C energy spectrum (black) versus two simulated spectra, one with the $S2$ tails modeled (red) and one without (blue). The data shown are taken from the full WIMP-search fiducial volume corresponding to electron drift times of 40 to 300 microseconds.

The additional tail area for a chosen event is drawn from an exponential distribution whose mean is proportional to uncorrected $S2$ size. This model of the $S2$ tails is generated using three steps and three fitting parameters, which are assumed to be independent of position, energy, and field. First, a "true" g_2 value ($g_{2,\mathrm{true}}$) is used to generate an initial set of tail-less MC events. The value of $g_{2,\mathrm{true}}$ is less than the one measured above, since the observed value of g_2 includes both the true $S2$ area, as well as the tail area. Next, a fraction of events, R, is selected to be assigned additional tail area. Finally, for each of the selected events, a random number of tail electrons is drawn from an exponential distribution with a mean of $b \cdot n_{e,LS}$, where b is a fitting parameter, and $n_{e,LS}$ is the number of simulated electrons that reach the liquid surface. The parameters are tuned in order to reproduce the energy spectrum of the ^{37}Ar and ^{131m}Xe data. The best fit values of b, R, and $g_{2,\mathrm{true}}$ are found to be $0.112(\pm 0.003)$, $0.73(\pm 0.02)$, and $17.60(\pm 0.05)$, respectively.

Figures 3 and 4 show the best fit spectra for ^{37}Ar and ^{131m}Xe. Figures 5 and 6 show the best fit model applied to ^{3}H and ^{14}C, respectively. The agreement of all of the simulated spectra with data is significantly improved after the addition of the tail model. The ^{37}Ar MC spectrum overpredicts the amplitude of the data at low energy (<2 keV); however, the same discrepancy is not observed in the ^{3}H spectrum.

E. Recombination fluctuations

The fluctuations in the recombination fraction, σ_R, are known to deviate significantly from those of a binomial process [10,26,31]. In Ref. [10] we reported that the fluctuations are approximately linear in n_i with a slope of about 0.067 quanta per ion. We do not attempt to obtain an absolute measurement of σ_R using the post-WS data because the $S2$ tails are correlated with the recombination fluctuations in nontrivial ways. The correlation makes it impractical to separate detector resolution and recombination fluctuations as was done for the WS2013 ^{3}H data. We instead apply an adjustment to the linear model and compare the resulting MC spectrum to data. We find the data are best described by a Gaussian adjustment to the linear model,

$$\sigma_R(r)^2 = r(1-r)\cdot n_i + \left(F_0 \exp\left(\frac{-(r-F_1)^2}{2F_2^2}\right)\right)^2 n_i^2, \quad (6)$$

where F_0, F_1 and F_2 are the constant fitting parameters,

$$\begin{aligned} F_0 &= 0.075 \pm 0.005, \\ F_1 &= 0.413 \pm 0.024, \\ F_2 &= 0.243 \pm 0.024. \end{aligned} \quad (7)$$

These parameters were optimized using post-WS ^{3}H and ^{14}C data using a grid search method described in Sec. 5.5.3 of Ref. [13]. A set of measurements of σ_R from Ref. [31] was also used to help constrain the low-recombination side of the model. When N_i is large and r is close to F_1, Eq. (6) reduces to a linear model with a slope of $0.075(\pm 0.005)$ quanta per ion. The first term on the right side of Eq. (6) mimics a binomial variance and prevents σ_R from going to 0 at extreme values or r. In our best fit model, the binomial term is negligible across the range of energies and fields tested.

The width of the MC spectra is compared to data in Fig. 7. We find that by adding the $S2$ tail model described in Sec. IV D and a model of recombination fluctuations that follows Eq. (6) to our simulation, we are able to reproduce the widths of the $S1$ and $S2$ spectra for ^{14}C β-decay events across all of the electric fields tested. Figure 8 shows a

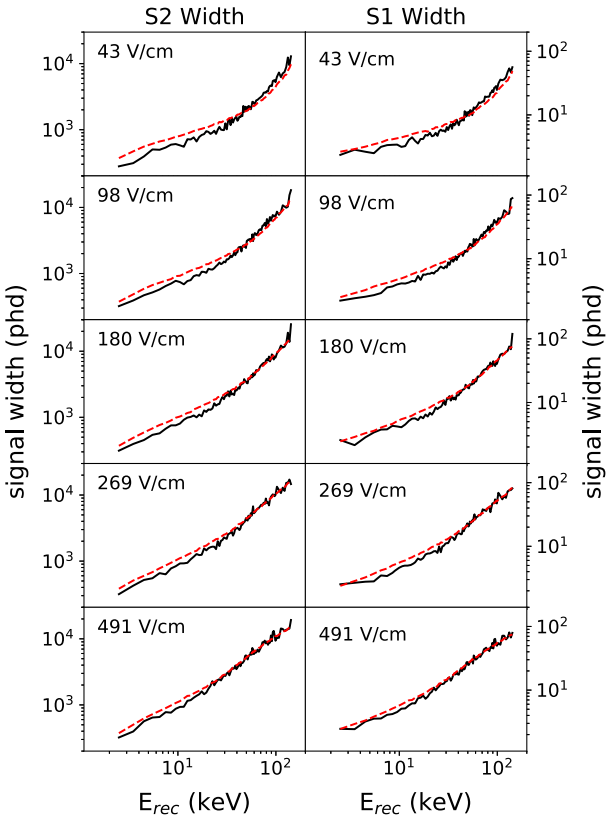

FIG. 7. This figure shows the best fit Gaussian width of the ^{14}C $S1$ (right) and $S2$ (left) bands for a selection of electric field bins. In these plots, the red dashed lines indicate simulated widths using the model described in Secs. IV D and IV E, while the black lines indicate the widths observed in data.

comparison to the σ_R measurements from WS2013. We find the new model matches data better than the linear model. The upward kink in the WS2013 measurements at 16 keV is due to an error that is described in Sec. V B.

There is still tension remaining between simulated and measured widths with this new model included. It may be that this is due to an underlying field dependence in the recombination fluctuations that has not been accounted for. This would be a third-order effect in our measurements of the yields, and we are able to reproduce the measured ^{3}H and ^{14}C spectra without accounting for this possible field dependence. We therefore elect to proceed using the model as described above.

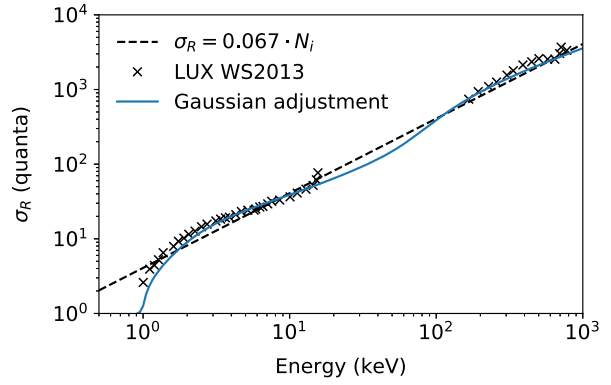

FIG. 8. Comparison of the recombination model developed in Sec. IV E (blue line) to the model from [10] (black dashed line). The black markers indicate the σ_R data presented in [26].

V. RESULTS AND DISCUSSION

A. Photon-electron fraction

Assuming that for ER the total number of generated quanta is fixed, as described in Sec. IV B, we can reduce L_y, Q_y, and r to a single quantity,

$$\rho \equiv \frac{n_\gamma}{n_e}. \tag{8}$$

Using the relations

$$L_y \equiv \frac{n_\gamma}{E}, \qquad Q_y \equiv \frac{n_e}{E}, \quad \text{and} \quad L_y + Q_y = \frac{1}{W}, \tag{9}$$

we can reconstruct the individual yields from ρ,

$$L_y = \frac{1}{W}\frac{\rho}{1+\rho} \quad \text{and} \quad Q_y = \frac{1}{W}\frac{1}{1+\rho}. \tag{10}$$

Further, using the relations

$$n_Q = (1+\alpha)n_i = (1+\rho)n_e \quad \text{and} \quad r = \frac{n_i - n_e}{n_i}, \tag{11}$$

where n_Q is the total number of quanta, we can reconstruct the average recombination probability,

$$r = \frac{\rho - \alpha}{1+\rho}. \tag{12}$$

Here we report the measured results of $\rho \equiv n_\gamma/n_e$. Figure 9 shows the results for post-WS ^{14}C, and Fig. 10 shows the results for post-WS ^{3}H. The measurements of n_γ and n_e, along with the reconstructed energy, have been numerically desmeared following the procedure laid out in Sec. IV A, using the model described in Secs. IV D and IV E. The sizes of these smearing corrections are taken as systematic uncertainty on their respective measurements. The uncertainties in g_1 and g_2 are also included in the systematic error. The systematic uncertainties are combined in quadrature and are shown as the light gray error bars in Figs. 9 and 10. The statistical fitting uncertainty and the uncertainty due to bin width are shown as the black error bars.

B. Discussion

Our results are in good agreement with previous measurements from WS2013, as is shown in Fig. 11. In this figure we compare measurements of Q_y from WS2013 ^{3}H [10] and from the ^{127}Xe electron capture [11,12] with those

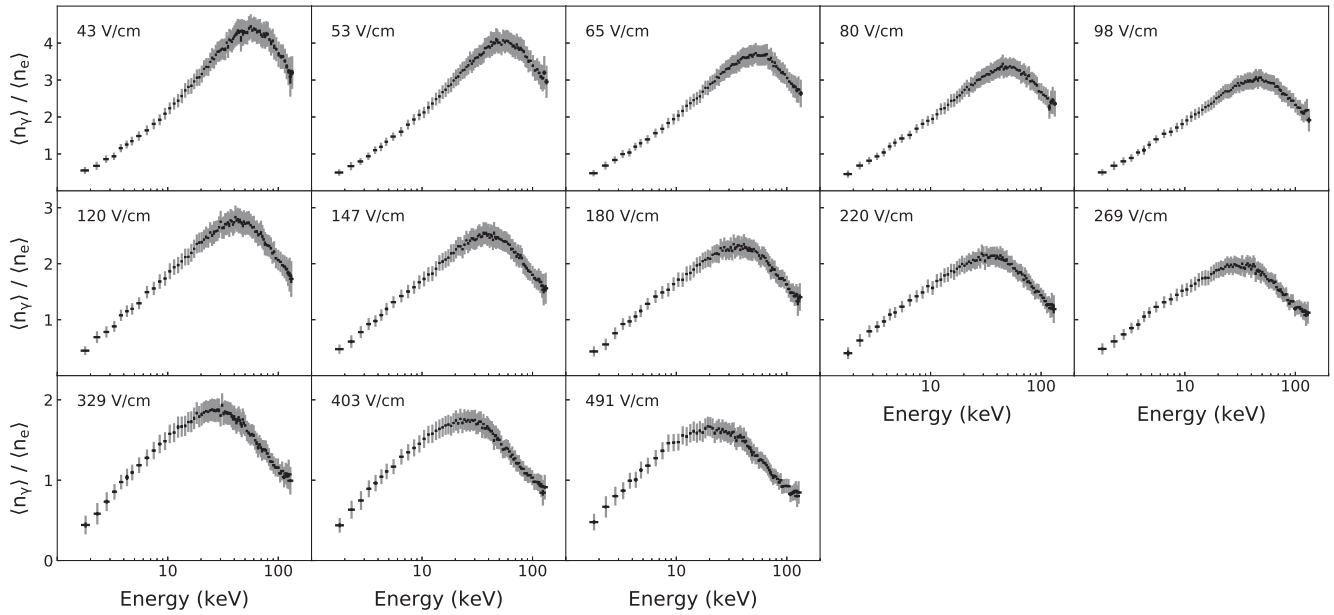

FIG. 9. Measurements of $\langle\rho\rangle$ for post-WS ^{14}C data in the specified electric field bins. The dark error bars show the statistical uncertainty, and the light error bars show the systematic plus statistical uncertainty.

from this work at similar electric fields. We find that the measurements agree within systematic error. When comparing our measurements of Q_y from interactions of β's in LXe to those from the ^{83m}Kr and ^{131m}Xe decays we find a disagreement of about 2-σ [12]. This is likely due to a difference in yields between β-decay interactions and those involving composite decays (such as ^{83m}Kr) or photoabsorption [7].

It should be noted that the results we present here are in disagreement with our previous ^{3}H yields and recombination measurements from Ref. [10] above 16 keV. In the previous work, an error in the implementation of the energy smearing correction resulted in some of the data being overcorrected. The error has only a minimal effect for most of the results reported in Ref. [10], but it is manifest at the end point of the tritium spectrum as a kink in the yields.

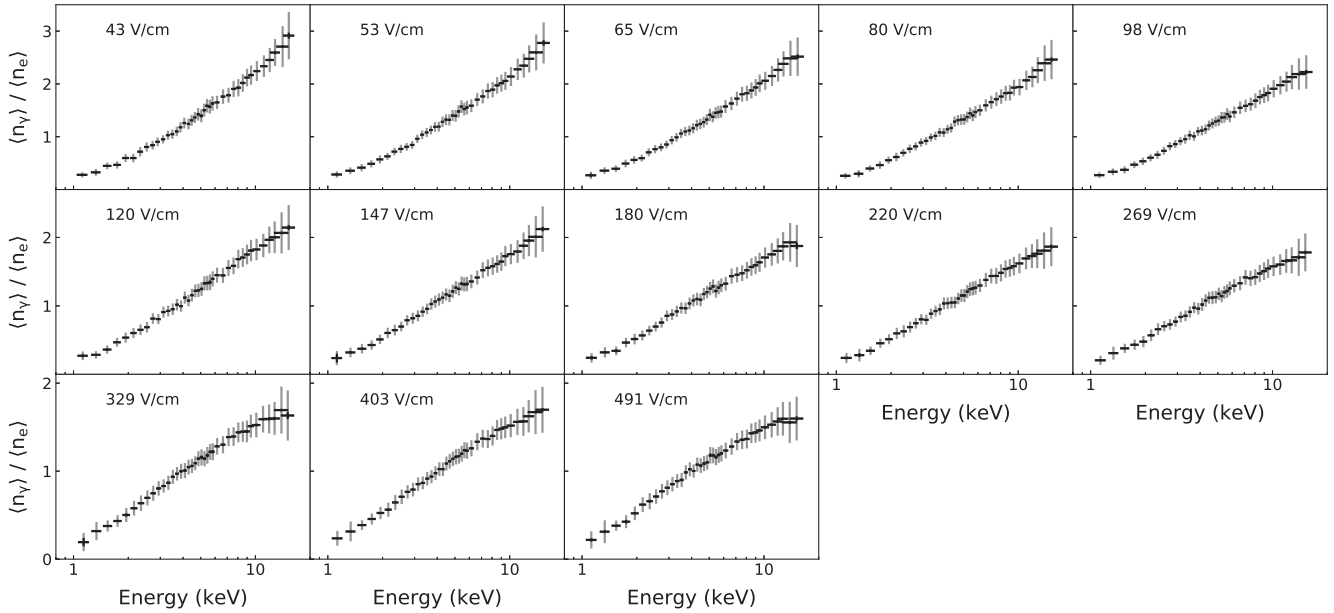

FIG. 10. Measurements of $\langle\rho\rangle$ for post-WS ^{3}H data in the specified electric field bins. The dark error bars show the statistical uncertainty, and the light error bars show the systematic plus statistical uncertainty.

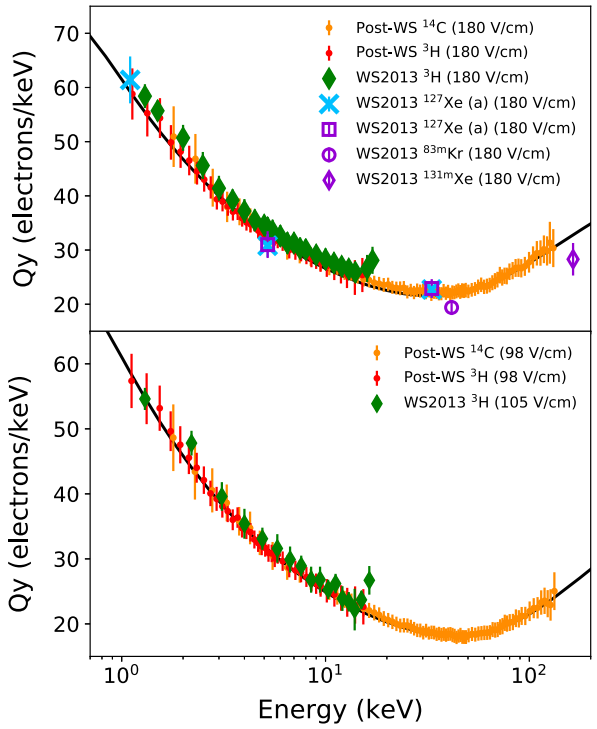

FIG. 11. Comparison of LUX post-WS Q_y measurements using ^{3}H (red) and ^{14}C (orange) to WS2013 measurements, which were taken at 105 and 180 V/cm. The green diamonds show the WS2013 ^{3}H measurements [10], and the blue X's and open magenta squares indicate WS2013 measurements of Q_y from ^{127}Xe electron capture [11,12]. The open circles and diamonds indicate WS2013 measurements of Q_y from the ^{83m}Kr and ^{131m}Xe decays, respectively [12]. The black line shows the final model used to generate the smearing corrections [13].

A detailed discussion of this error can be found in Sec. 5.3.2 of Ref. [13].

VI. SUMMARY

We have presented improved measurements of the response of liquid xenon to β decays in the LUX detector, which were taken after WS2014-2016 was completed. We describe the various sources used, along with the timeline and the respective activities of the calibrations. We use the ^{83m}Kr and ^{131m}Xe lines to measure the average g_1 and g_2 efficiency factors and to characterize the positional variation thereof.

The ^{37}Ar and ^{131m}Xe calibration data are used to alter the existing model of detector resolution to account for the $S2$ tail pathology in the $S2$ spectra. We used this updated model to numerically calculate the effect of smearing on the ^{3}H and ^{14}C β-decay spectra. We also found it necessary to update the empirical model of recombination fluctuations presented in [10] to better match the data above 20 keV.

We present measurements of the photon-to-electron ratio of β events in liquid xenon from ^{3}H and ^{14}C. These measurements can be used to calculate the charge yield, light yield, and recombination probability over a wide range of electric fields and energies. This is the most extensive data set of the quantities for β decay in liquid xenon, and is directly relevant for understanding the dominant background in future dark-matter experiments.

ACKNOWLEDGMENTS

This work was partially supported by the U.S. Department of Energy (DOE) under Awards No. deFG02-08ER41549, No. deFG02-91ER40688, No. deFG02-95ER40917, No. deFG02-91ER40674, No. deNA0000979, No. deFG02-11ER41738, No. deSC0006605, No. deAC02-05CH11231, No. deAC52-07NA27344, No. deSC0019066, and No. deFG01-91ER40618; the U.S. National Science Foundation under Grants No. PHYS-0750671, No. PHY-0801536, No. PHY-1004661, No. PHY-1102470, No. PHY-1003660, No. PHY-1312561, and No. PHY-1347449; the Research Corporation Grant No. RA0350; the Center for Ultralow Background Experiments in the Dakotas (CUBED); and the South Dakota School of Mines and Technology (SDSMT). LIP-Coimbra acknowledges funding from Fundação para a Ciência e a Tecnologia (FCT) through the Grant No. PTDC/FIS-PAR/28567/2017. Imperial College and Brown University thank the United Kingdom Royal Society for travel funds under the International Exchange Scheme (Grant No. IE120804). The United Kingdom groups acknowledge institutional support from Imperial College London, University College London and Edinburgh University, and from the Science & Technology Facilities Council for PhD studentship Grant No. ST/K502042/1 (A. B.). The University of Edinburgh is a charitable body, registered in Scotland, with registration number SC005336. This research was conducted using computational resources and services at the Center for Computation and Visualization, Brown University. We gratefully acknowledge the logistical and technical support and the access to laboratory infrastructure provided to us by the SURF and its personnel in Lead, South Dakota. SURF was developed by the South Dakota Science and Technology Authority, with an important philanthropic donation from T. Denny Sanford, and is operated by Lawrence Berkeley National Laboratory for the Department of Energy, Office of High Energy Physics.

[1] D. S. Akerib *et al.* (LUX Collaboration), Nucl. Instrum. Methods Phys. Res., Sect. A **704**, 111 (2013).
[2] D. S. Akerib *et al.* (LUX Collaboration), Phys. Rev. Lett. **112**, 091303 (2014).
[3] D. S. Akerib *et al.* (LUX Collaboration), Phys. Rev. Lett. **116**, 161301 (2016).
[4] D. S. Akerib *et al.* (LUX Collaboration), Phys. Rev. Lett. **118**, 021303 (2017).
[5] E. Aprile *et al.* (XENON Collaboration 7), Phys. Rev. Lett. **121**, 111302 (2018).
[6] X. Cui *et al.* (PandaX-II Collaboration), Phys. Rev. Lett. **119**, 181302 (2017).
[7] M. Szydagis, A. Fyhrie, D. Thorngren, and M. Tripathi, J. Instrum. **8**, C10003 (2013).
[8] B. J. Mount *et al.*, arXiv:1703.09144.
[9] D. S. Akerib *et al.* (LUX-ZEPLIN Collaboration), arXiv:1802.06039.
[10] D. S. Akerib *et al.* (LUX Collaboration), Phys. Rev. D **93**, 072009 (2016).
[11] D. S. Akerib *et al.* (LUX Collaboration), Phys. Rev. D **96**, 112011 (2017).
[12] D. S. Akerib *et al.* (LUX Collaboration), Phys. Rev. D **95**, 012008 (2017).
[13] J. Balajthy, Purity monitoring techniques and electronic energy deposition properties in liquid Xenon time projection chambers, Ph.D. thesis, Uniersity of Maryland, 2018.
[14] V. V. Kuzminov and N. J. Osetrova, Phys. At. Nucl. **63**, 1292 (2000).
[15] F. E. Wietfeldt, E. B. Norman, Y. D. Chan, M. T. F. da Cruz, A. García, E. E. Haller, W. L. Hansen, M. M. Hindi, R.-M. Larimer, K. T. Lesko, P. N. Luke, R. G. Stokstad, B. Sur, and I. Žlimen, Phys. Rev. C **52**, 1028 (1995).
[16] E. Aprile and T. Doke, Rev. Mod. Phys. **82**, 2053 (2010).
[17] D. S. Akerib *et al.* (LUX Collaboration), J. Instrum. **13**, P02001 (2018).
[18] D. S. Akerib *et al.* (LUX Collaboration), J. Instrum. **12**, P11022 (2017).
[19] L. W. Kastens, S. Bedikian, S. B. Cahn, A. Manzur, and D. N. McKinsey, J. Instrum. **5**, P05006 (2010).
[20] L. W. Kastens, S. B. Cahn, A. Manzur, and D. N. McKinsey, Phys. Rev. C **80**, 045809 (2009).
[21] D. S. Akerib *et al.* (LUX Collaboration), Phys. Rev. D **96**, 112009 (2017).
[22] J. R. Verbus *et al.*, Nucl. Instrum. Methods Phys. Res., Sect. A **851**, 68 (2017).
[23] D. S. Akerib *et al.* (LUX Collaboration), arXiv:1608.05381.
[24] E. Boulton, E. Bernard, N. Destefano, B. Edwards, M. Gai, S. Hertel, M. Horn, N. Larsen, B. Tennyson, C. Wahl, and D. McKinsey, J. Instrum. **12**, P08004 (2017).
[25] Moravek Biochemical Brea California 92821 U.S.A.
[26] A. Dobi, Measurement of the electron recoil band of the LUX dark matter detector with a Tritium calibration source, Ph. D. thesis, Uniersity of Maryland, 2014.
[27] M. Szydagis, N. Barry, K. Kazkaz, J. Mock, D. Stolp, M. Sweany, M. Tripathi, S. Uvarov, N. Walsh, and M. Woods, J. Instrum. **6**, P10002 (2011).
[28] B. Lenardo, K. Kazkaz, A. Manalaysay, J. Mock, M. Szydagis, and M. Tripathi, IEEE Trans. Nucl. Sci. **62**, 3387 (2015).
[29] E. Aprile and T. Doke, Rev. Mod. Phys. **82**, 2053 (2010).
[30] R. Platzman, Int. J. Appl. Radiat. Isotopes **10**, 116 (1961).
[31] C. E. Dahl, The physics of background discrimination in liquid xenon, and first results from Xenon10 in the hunt for WIMP dark matter., Ph.D. thesis, Princeton University, 2009.
[32] T. Doke, A. Hitachi, J. Kikuchi, K. Masuda, H. Okada, and E. Shibamura, Jpn. J. Appl. Phys. **41**, 1538 (2002).